Batteries & Supercaps

Articles
doi.org/10.1002/batt.202100026

Chemistry
Europe
European Chemical
Societies Publishing

# Sodium-Ion Battery Full-Cell Study with a Pseudocapacitive MoSe$_2$-Porous N-Doped Carbon Composite Anode and Intercalated Sodium Vanadium Fluorophosphate Cathode

Amlan Roy,[a] Ananta Sarkar,[b] Md. Adil+,[a] Supriya Sau+,[a] N. Abharana,[c] and Sagar Mitra*[a]

Despite higher conductivity and larger d-spacing (0.65 nm) of MoSe$_2$ compare to its analogous MoS$_2$ and higher theoretical capacity (~422 mA h g$^{-1}$) compare to commercially available graphite, it experiences high volume expansion, sheets agglomeration during cycling, which limits their capacities and high rate application. Herein, we have shown interest in MoSe$_2$ materials as analogous to MoS$_2$ anode and grown MoSe$_2$ nanosheets on the nitrogen-doped carbon followed by covered with reduced graphene oxides sheets (NC@MoSe$_2$@rGO) composite through a simple solvothermal synthesis followed by annealing treatment. The porous NC compound could bring several advantages like, it can reserve a sufficient amount of electrolyte for easy access of Na-ion diffusion. Increasing the conductivity by introducing the doping of nitrogen on the NC structure and simultaneously rGO can reduce the volume expansion of MoSe$_2$ during the cyclic performance. Ex-situ XANES and XPS technique explored the sodiation mechanism of the NC@MoSe$_2$@rGO composite. It has been found the irreversible conversion of MoSe$_2$ after 1$^{st}$ cycle by converting the discharged products of Mo and Na$_2$Se. The NC@MoSe$_2$@rGO anode is connected with electrolyte and a high potential Na$_3$V$_2$O$_2$(PO$_4$)$_2$F (NVOPF) to acquire potential applications' approval cathode material. The full-cell delivers a voltage of operation at 2.1 V with high specific capacity of ~176 mA h g$^{-1}$ (current rate of 0.05 A g$^{-1}$) with an energy density of ~369.6 W h/kg $_{anode}$ at 20 °C.

## 1. Introduction

MoSe$_2$, a class of transition metal dichalcogenides (TMDs), have achieved great success in several fields such as energy storage,[1–5] photocatalysis,[6,7] optoelectronics,[8] etc. It possesses higher d-spacing (~0.65 nm), higher electronic

conductivity of selenium[9] (10$^{-3}$ s m$^{-1}$) vs S (5×10$^{-28}$ s m$^{-1}$) in MoS$_2$, which makes MoSe$_2$ as a promising anode material especially in case of sodium-ion battery.[10–12] However, insufficient charge transfer kinetics and massive volume changes of active material during insertion/de-insertion of sodium-ion leading to capacity fading, poor rate performances, low Coulombic efficiency as reported for other TMDs.[10,13–16] At the same time, after the first cycle, the reaction center shifted from MoSe$_2$ to Na$_2$Se, where Polyselenide dissolution raises a primary concern for the utilization of active material during different cycling.[17–19]

Several approaches have deployed to achieve the issues mentioned above by introducing conductive 0D, 1D, 2D carbon materials into the electrode. For example, oleic acid functionalized polydopamine[20] has been used as a carbon source, intercalated in between the MoSe$_2$ layers during hydrothermal synthesis. Thus, the MoSe$_2$@C anode exhibits a reversible capacity of 367 mA h g$^{-1}$ at a high current rate of 5.0 A g$^{-1}$ with 100 cycles stability. Li et al.[20] An expanded (002) layers of MoSe$_2$/C$_{cas}$ enhance the conductivity and restrict the MoSe$_2$ aggregation and volume expansion. As a result, obtained reversible capacity was 360 mA h g$^{-1}$ at a current density of 0.5 A g$^{-1}$. Yang et al.[21] Synthesized ascorbic acid derived carbon, which was coated uniformly on MoSe$_2$ during hydrothermal synthesis. It can give the capacity of 395 mA h g$^{-1}$ at 1.0 A g$^{-1}$ current rate up-to 100 cycles. MoSe$_2$ grown on the ammonium citrate[22] derived nitrogen-doped carbon (MoSe$_2$/CN) have also adequately reported as an anode with excellent cycling stability and high rate capability for SIB. These results imply the enhancement of sodium storage performance by introducing carbon-based composites. However, in practical application, volume changes of MoSe$_2$ during cycling remain an open challenge by using the minimum amount of conductive carbon and optimizing cyclic stability.

Metal-organic frameworks (MOFs) are porous material with a high surface area, composed of Metal-ions covalently linked with organic components.[23–25] The organic units in MOF create a three-dimensional structure while bonding with metal ions, e.g., Zn$^{2+}$, Co$^{2+}$, Al$^{3+}$, and produces high surface area ranging from 800 to 3400 m$^2$ g$^{-1}$.[23] It has several applications due to

[a]  A. Roy, M. Adil,+ S. Sau,+ Prof. S. Mitra
     Electrochemical Energy Laboratory,
     Department of Energy Science and Engineering
     Indian Institute of Technology Bombay
     Powai, Mumbai400076, India
     E-mail: sagar.mitra@iitb.ac.in
[b]  Dr. A. Sarkar
     Department of Chemical Engineering
     National Institute of Technology Durgapur
     Durgapur 713209, India
[c]  N. Abharana
     Atomic & Molecular Physics Division
     Bhabha Atomic Research Centre,
     Mumbai 400085, India
[+]  These authors contributed equally to this work.

Check for updates

the increased surface area with tunable pore sizes.[25,26] The MOFs can quickly transform to hetero-atom doped porous carbon during the calcination process at a high temperature in an inert atmosphere.[27] Thus, it can provide a sufficient path to reduce the diffusion of $Na^+/Li^+$ and increase materials specific storage capacity.[28–30]

Herein, we report the fabrication of $MoSe_2$ nanosheets on Zeolite imidazole framework (ZIF-8) derived N-doped carbon polyhedral (NC), after that covered with conductive rGO through the simple solvothermal method (later termed as NC@MoSe$_2$@rGO). The unique heterostructures of NC@Mo-Se$_2$@rGO can overcome some of the shortcomings of $MoSe_2$ as follows: firstly, the porous carbon can allow the electrolyte throughout the electrode and provide a shorter diffusion path length for sodium-ion. Secondly, dual protection with carbon layers prevent the stacking/restacking and can accommodate the volume expansion of $MoSe_2$ during the charge/discharge process.[19] Thirdly, nitrogen-doped on the carbon polyhedral and rGO not only increases the overall conductivity of the electrode but prevent the poly-selenide dissolution issues after the first cycle; thus, active material utilization will be more. When NC@MoSe$_2$@rGO tested against Na/Na$^+$, it exhibits superior electrochemical performance with a reversible capacity of $\sim 391.84$ mAh g$^{-1}$ at a current density of 100 mA g$^{-1}$ and stable up-to 120 cycles and also provided excellent rate performances. We choose $Na_3V_2O_2(PO_4)_2F$ (NVOPF) as a cathode material to make a sodium-ion full-cell battery with high nominal potential. The NC@MoSe$_2$@rGO//NVOPF full-cell showed the high specific capacity of $\sim 176$ mAh g$^{-1}$ with a capacity retention of $\sim 83\%$ after 100$^{th}$ cycle the potential window of 1.5 V–3.5 V at 20 °C. This full-cell exhibits a high energy density of $\sim 369.6$ Wh kg$^{-1}$ at a current rate of 0.05 A g$^{-1}$ with the nominal potential 2.1 V.

## 2. Results and Discussion

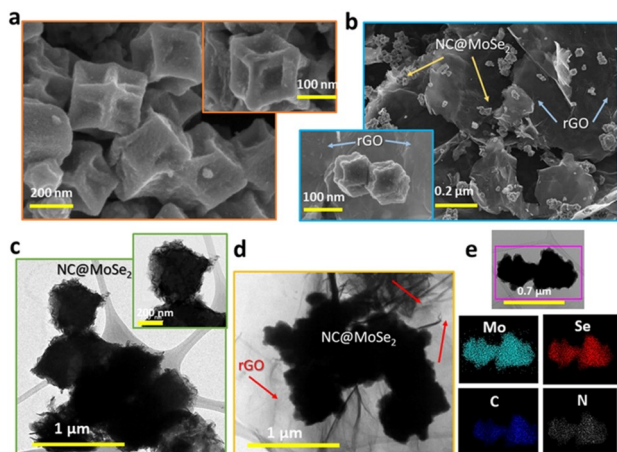### 2.1. Characterization of NC@MoSe$_2$@rGO Anode and NVOPF Cathode

The capacity fading issue in the conversion-based materials is the major concern for sodium-ion battery (SIB). This report's ultimate goal was to prepare unique 3-D structured anode material that can prevent volume expansion and provide a shorter diffusion path length of sodium by introducing the conductivity during the SIB cycling process. A schematic is shown in Figure 1a to understand the synthesis mechanism of the NC@MoSe$_2$@rGO composites. Firstly, we used Zn-source and organic 2-methyl imidazole to prepare ZIF-8 and heated to 850 °C to prepared N-doped carbon (NC). Then, the NC powder was dispersed in a glucose-containing Mo-source solution to form a black color suspension mixed with Se-N$_2$H$_4$. The absorbed anionic species of Mo—O on the carbon surface is supposed to be deposited and reduced to Mo$^{4+}$ in the presence of hydrazine hydrate during a simple solvothermal process at 200 °C for 12 hr. After that, thermal annealing was done at a high temperature of 800 °C in the inert atmosphere
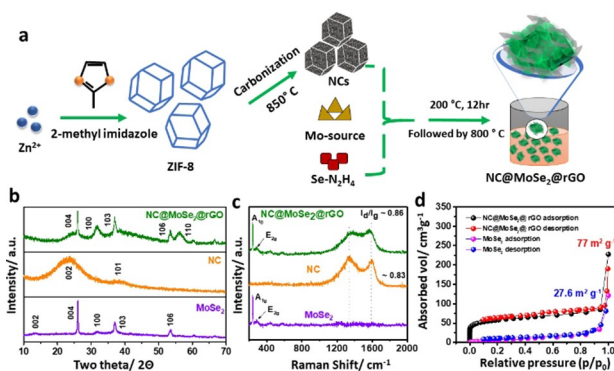


**Figure 1.** a) Schematic illustration for the synthesis of NC@MoSe$_2$@rGO; b) powder X-ray diffraction pattern; c) Raman study, and d) nitrogen adsorption/desorption isotherms of the MoSe$_2$ and NC@MoS$_2$@rGO composite, respectively.

to get the final composite of NC@MoSe$_2$@rGO. The powder X-ray diffraction (XRD) used to check the crystalline phase of as-prepared NC@MoSe$_2$@rGO composites. The XRD pattern of as-synthesized powder showed (Figure 1 (b)) the characteristic peaks at $2\theta = 26.1°$, 31.5°, 37.3°, 53.5° and 56.1° corresponding to diffraction planes of (004), (100), (103), (106) and (110) for MoSe$_2$ in NC@MoSe$_2$@rGO (JCPDS#29-0914), respectively. The lower shift of (004) peak and disappearance of (002) and (110) planes were found in NC@MoSe$_2$@rGO compared to MoSe$_2$. This attributed to the amorphous carbon formed during solvothermal synthesis because glucose present in the solution can inhibit the growth of MoSe$_2$ along c-direction similar to MoS$_2$ nanosheets as reported previously,[31] or it contains few layers to detect by XRD[32,33] Figure1c shows the Raman spectrum of MoSe$_2$, NC and NC@MoSe$_2$@rGO composites to know about the bonding between various atoms in the structure. The Raman peaks at $\sim 241$ and $\sim 284$ cm$^{-1}$ corresponding to A$_{1g}$ and E$_{2g}$ mode of MoSe$_2$, respectively.[34] Simultaneously, $sp^2$-hybridized carbon is found in as-prepared composite through the I$_d$/I$_g$ ratio calculation.[35] The I$_d$/I$_g$ ratio is $\sim 0.83$ for carbon compound and $\sim 0.86$ for composite with D- and G- band at 1132 cm$^{-1}$ and 1568 cm$^{-1}$. N$_2$ adsorption experiment was performed for surface area (BET) calculation of the bare MoSe$_2$ and NC@MoSe$_2$@rGO composites. Figure 1d shows the calculated surface area of MoSe$_2$ was increased from 27.6 m$^2$ g$^{-1}$ for MoSe$_2$ to 77 m$^2$ g$^{-1}$ for NC@MoSe$_2$@rGO composites. The increase of the surface area of MoSe$_2$ after incorporation of the NCs/rGO compound may be due to its large surface area, which can act as a supporting matrix for the consistent growth of MoSe$_2$. In NC@MoSe$_2$@rGO, the larger surface area can be beneficial for more accessibility of the electrolyte to the electrode interface; it can decrease the sodium ion diffusion and help achieve the stable electrochemical performance of the anode. Scanning electron microscopy (SEM) and Transmission electron microscopy (TEM) were used for morphological investigation of as-prepared composites. Figure 2(a) and (b) shows the uniform distribution of MoSe$_2$ on NC compound (NC@MoSe$_2$) and NC@MoSe$_2$@rGO composites, respectively. This unique morphology can be

**Figure 2.** Morphological characterization of NC@MoSe$_2$ and NC@MoSe$_2$@rGO anode, SEM of a) NC@MoSe$_2$ compound with uniform polyhedral shape, b) randomly distributed NC@MoSe$_2$ composite on rGO in NC@MoSe$_2$@rGO. TEM images of c) NC@MoSe$_2$, d) NC@MoSe$_2$@rGO, e) elemental mapping of the NC@MoSe$_2$@rGO composites displaying the homogeneous distribution of Mo. Se, N, and C throughout the sample.



**Figure 3.** X-ray photoelectron spectra of the NC@MoSe$_2$@rGO composite with survey spectrum (a) as well as high-resolution spectra of Se3d (b), Mo3d (c), C1s (d), N1s (e), and O1s (f), respectively.

correlated with SEM and TEM images of the NC compounds, as shown in Figure S1a and b, respectively. The NC carbon contains many layers staking together to form a uniform polyhedral with a sharp edge (Figure S1b). In general, during solvothermal synthesis at 200 °C, bulk MoSe$_2$ layers decorated randomly (Figure S1c) and created morphology very similar to flower-type. After adding the NC compound, growth of the MoSe$_2$ happened on the rough surface of the NC compound in NC@MoSe$_2$ composites (Figure 2c and Figure S1d). As

Observed in the HRTEM image (Figure S1e, inset), the MoSe$_2$ nanosheets having very few-layers ($<$10 layers) stacked together with the expanded d-spacing ($\sim$0.67 nm) of (002) planes. Figure 2d and Figure S1f shows the composite of NC@MoSe$_2$ on the rGO sheets. The advantage of using rGO in this particular structure is to enlarge the contact area of electrode-electrolyte, decrease Na$^+$ diffusion length. The distribution of different elements throughout the samples was characterized by energy-dispersive X-ray spectroscopy (EDAX), as shown in Figure 2e. Elemental mapping analysis confirms the uniform distribution of Mo, Se, C, and N in NC@MoSe$_2$@rGO composites. To quantify the loading amount of MoSe$_2$ in the NC@MoSe$_2$@rGO composite, we had done TGA analysis where samples were heated from RT to 800 °C in an air atmosphere with the scan rate of 10 °C/min. The first weight loss below 200 °C because of the physically absorbed water molecules in both samples. The subsequent weight loss above 300 °C due to the oxidation products like- SeO$_2$, MoO$_3$ and oxidation of carbon[36] present in the samples, as shown in Figure S2a. Thus, the loading amount of MoSe$_2$ in the composite of NC@MoSe$_2$@rGO was calculated to be almost $\sim$70%.

X-ray photoelectron spectroscopy (XPS) and FTIR were performed to understand the interaction mechanism and chemical composition with oxidation states of the as-prepared NC@MoSe$_2$ composites. It is believed that the oxygen functional groups (such as hydroxyl, carboxyl, carbonyl etc.) present
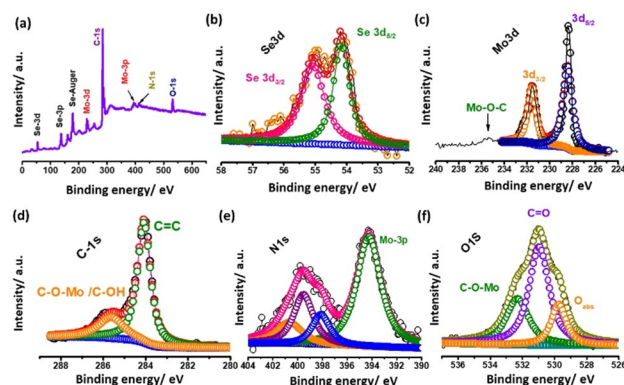
on the GO sheets can act as a host material for NC@MoSe$_2$ through electrostatic interaction. Furthermore, as an example, we can estimate the force constant for such interaction due to different functional groups present in the rGO sheets after the NC@rGO composite. As shown in Figure S2b, FTIR for sample rGO and NC@MoSe$_2$@rGO, the −OH stretching vibration has increase from 3425.9 cm$^{-1}$ (rGO) to 3434.7 cm$^{-1}$ (NC@MoSe2@r-GO) and diminish of C=O bond in the final product confirms the electron donation from oxygen to Mo during the synthesis process.[37] The calculated bond constant for −OH bonds are 642 N/m and 645.3 N/m for rGO and NC@MoSe$_2$@rGO, respectively. The full scan of XPS spectra demonstrates Se, Mo, C, N, and O elements are shown in Figure 3a. The Se wide scan shows (Figure 3b) two peaks, at 53.9 and 54.8 eV, represents 3d$_{5/2}$ and 3d$_{3/2}$, respectively, which is consistent with (-II) oxidation state of Se. Mo 3d exhibits two main peaks at 231.0 eV and 228.4 eV, which corresponded to Mo3d$_{3/2}$ and Mo3d$_{5/2}$ of Mo$^{6+}$ in MoSe$_2$ (Figure 3c).[11] Simultaneously, (+VI) oxidation state of Mo is at 235 eV, which is due to Mo−O−C bond's existence.[38] The C 1s peak at 284.1 eV for C=C due to the sp$^2$ nature of as-synthesized carbon from ZIF-8. The peak at 285.6 eV corresponds to C−O−Mo and C−OH bond, as shown in Figure 3d.[39,40] The high-resolution deconvoluted N 1s spectra (in Figure 3e) divided into three different peaks at 398.0 eV, 399.58 eV and 400.7 eV due to pyridinic N and pyrrolic N and graphitic N, respectively.[41] The presence of nitrogen reflects the successful doping of N during the carbonization of ZIF-8, which contains imidazole frameworks in the structure. As shown in Figure 3f, the O1s spectra were deconvoluted into three peaks at 532.3 eV, 531.2 eV, and 529.7 eV corresponding to C=O, C−O−Mo, and absorb oxygen, respectively.[42] The above data suggests Mo's bonding in MoSe$_2$ with oxygen atom presents in NC to form C−O−Mo bond. The existence of C−O−Mo bonds came from the oxygen functionality of NC with Mo ions. This would help restrict the volume expansion of layered structure and promote faster ion transport at the interface.[43]

**Batteries & Supercaps**

Articles
doi.org/10.1002/batt.202100026

**Chemistry Europe**
European Chemical
Societies Publishing

## 2.2. NC@MoSe₂@rGO Anode against Na/Na⁺ Half-Cell Study

To investigate the half-cell performances of NC@MoSe$_2$@rGO, MoSe$_2$, and NC, cyclic voltammograms (CV), galvanostatic charge-discharge (GCD) were carried out using 2032 type coin cell against Na/Na⁺ as a counter/reference electrode at 20 °C. Figure 4a and Figure S3a (inset) represents the CV plot of NC@MoSe$_2$@rGO and NC@MoSe$_2$ at a scan rate of 0.1 mV s⁻¹ within the potential window of 0.1 V to 2.6 V vs Na/Na⁺. During the reduction of NC@MoSe$_2$@rGO electrode, the first cathodic peak appeared at ~0.71 V, which corresponds to Na ion's intercalation in the MoSe$_2$ layers transform to Na$_x$MoSe$_2$.[17,44] The peak below 0.5 V (~0.45 V) always represents the conversion of intercalated sodium MoSe$_2$ to Mo and Na$_2$Se, followed by SEI formation.[45,46] During the positive voltage sweep, the broad peak appears at ~1.76 V and ~2.2 V, which is due to the conversion of Na$_2$Se to Se and poly-selenide formation, respectively.[17] Compared to NC@MoSe$_2$@rGO, the CV curve (first three cycles shown in the inset of Figure S3a) of NC@MoSe$_2$ shows the lower current responses with the two

reduction peaks at ~0.68 V and ~0.39 V during the first cycle. Simultaneously, faster sodium kinetics can be realized from smaller voltage hysteresis of NC@MoSe$_2$@rGO (~0.45 V) than NC@MoSe$_2$ (~0.63 V) after the first cycles. This reflects the faster sodium transport and higher reactivity of the electrode after incorporating rGO in the NC@MoSe$_2$ electrode.

The galvanostatic charge-discharge (GCD) was performed (Figure 4b) to understand the storage capacity of the material at a current rate of 100 mA g⁻¹. Like CV results, the first intercalation of sodium appears ~0.7 V followed by a sloppy region up to 0.1 V. This is due to the conversion of anode followed by SEI layer formation on the anode surface, as discussed above. The NC@MoSe$_2$@rGO electrode exhibits a first discharge capacity of ~638.1 mA h g⁻¹ with a Coulombic efficiency of ~66.7 %, the more sodium consumption during the first cycle attributed due to the trapping of sodium-ion in-between the carbon layers of NC and rGO and formation of SEI layer.[47] But Coulombic efficiency has been improved to ~99.6 % with the reversible capacity of ~391.8 mA h g⁻¹ up to 120 cycles, which is compared with other existing literature as
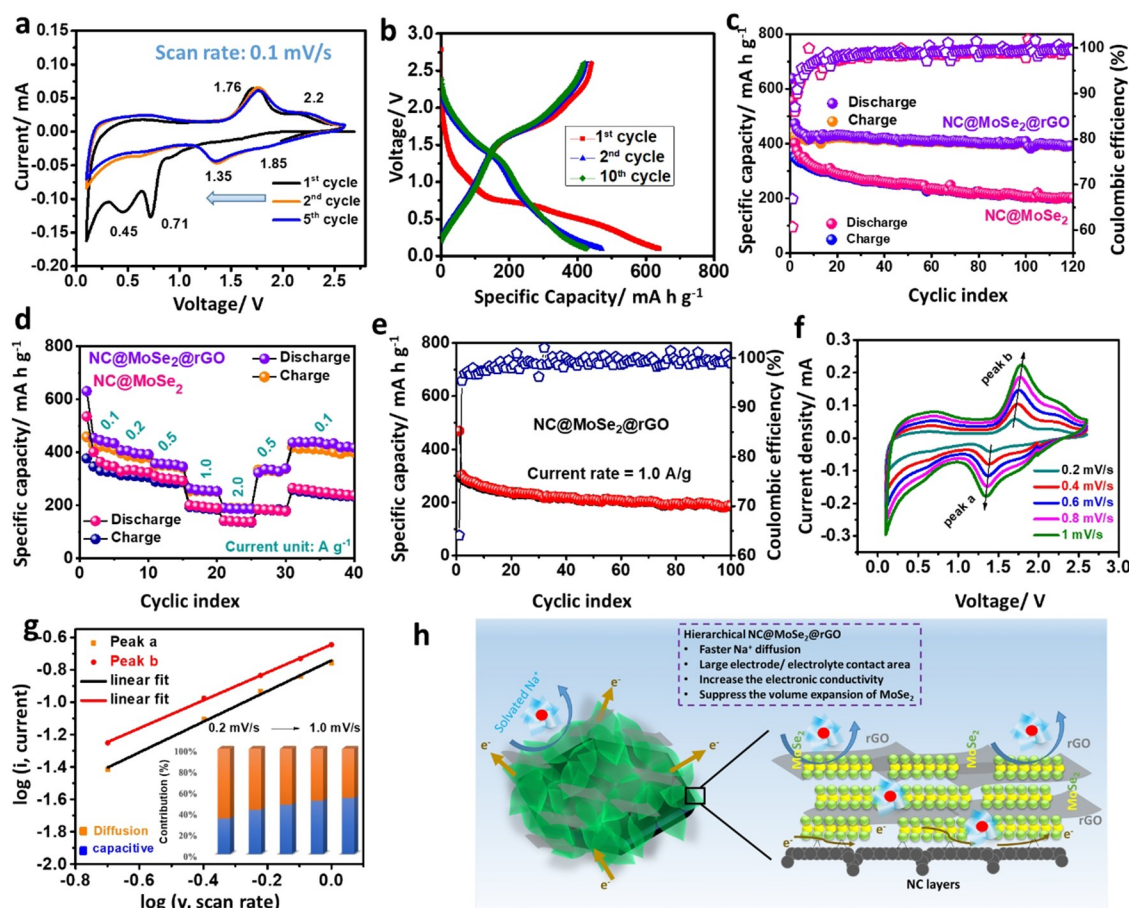


**Figure 4.** Electrochemical performances of NC@MoSe$_2$@rGO anode at 20 °C. a) CV plot between the potential range of 0.1 and 2.6 V. b) Discharge/charge voltage vs. specific capacity plot at a current rate of 100 mA g⁻¹. c) Comparison cycling performance of NC@MoSe$_2$@rGO at a current rate of 1.0 A g⁻¹. d) the rate capability at different current densities from 100 mA g⁻¹ to 2 A g⁻¹. e) Long-term cycling performance of NC@MoSe$_2$@rGO anode at a high current density of 1.0 A g⁻¹. f) CV plot at different scan rates ranging from 0.2 to 1.0 mV s⁻¹. g) corresponding log i vs. log v plots of redox peaks 1.3 V (peak a) and 1.8 V (peak b) of the anode (i = current, v = scan rate) (inset: Bar diagram corresponds to diffusion & capacitive nature of the anode with different scan rates). h) Schematic illustration of ion transport (Na⁺ and e⁻) during the charge/discharge process.

summarized in Table S6. The electrode consists of NC@MoSe$_2$ shows the initial capacity of 557.2 mAhg$^{-1}$ with the Coulombic efficiency of ~60.7% but retained only 202.6 mAhg$^{-1}$ after 120 cycles (Figure 4c and Figure S3a). In contrast, bare MoSe$_2$ was tested under the same potential window and a current rate (Figure S3b and c). The first discharge capacity of the only MoSe$_2$ was ~490.7 mAhg$^{-1}$ with a Coulombic efficiency of ~58%. However, the severe capacity decay was observed for MoSe$_2$ electrode. It shows the discharge capacity of ~35 mAhg$^{-1}$ after the 40th cycle only with capacity retention is only ~16% from its second cycle. Figure S3d and e show the GCD and cycling stability performance of only NC to investigate the actual contribution of NC in the NC@MoSe$_2$@rGO electrode. Pure NC offers the initial discharge capacities of ~432.2 mAhg$^{-1}$ with a Coulombic efficiency of ~28%. The high discharge capacity in the first cycle reveals the SEI layer formation on the NC surface. In contrast, capacity recovery was found from the second cycle with a discharge capacity of ~145.7 mAhg$^{-1}$ with an efficiency of ~78%. It shows the reversible capacity of ~116 mAhg$^{-1}$ and stable up-to 100 cycles. Therefore, the capacity contribution of NC in the NC@MoSe$_2$ electrode is only ~6−7 mAhg$^-$. The NC@MoSe$_2$@rGO exhibits higher capacity than NC@MoSe$_2$ and bare MoSe$_2$, indicating faster diffusion of sodium-ion through the defects of rich NC and rGO to the active materials. Figure 4(d) compares the power plot between NC@MoSe$_2$@rGO and NC@MoSe$_2$ at different current rates. The NC@MoSe$_2$ exhibited poor rate performance during the transition from high current 2.0 Ag$^{-1}$ to low current 100 mAg$^{-1}$. However, NC@MoSe$_2$@rGO shows much better rate performances at different current rates (100 mAg$^{-1}$) from low to high (1.0 and 2.0 Ag$^{-1}$). The long-term cycling performance of the anode is represented in Figure 4e. At a moderately high current density of 1.0 Ag$^{-1}$, the NC@MoSe$_2$@rGO delivers an initial capacity of 469 mAhg$^{-1}$ with a Coulombic efficiency of 64.0% and 186.4 mAhg$^{-1}$ after 100 cycles. The capacity and Coulombic efficiencies are higher than NC@MoSe$_2$ at a high rate, as shown in Figure S3f. To explore the improved, enhanced electrochemical performances, higher rate capability and better cyclic stability of NC@MoSe$_2$@rGO composite, CV was performed at various scan rates from 0.2 mVs$^{-1}$ to 1.0 mVs$^{-1}$ as shown in Figure 4f. It is well known that there is a non-linear relationship between peak current ($i$) and the square root of scan rate ($v$); $i = av^b$ Where $a$ and $b$ are constant. Generally, if the b-value near 0.5, then the discharge process is controlled by diffusion of ion and if it is near to value 1, then the process is controlled by pseudocapacitance.[48] At the same time, total current ($i(v)$) can divide into two parts: $i(v) = k_1v + k_2v^{0.5}$, where $i(v)$ is the current at the particular scan rate, $k_1v$ and $k_2v$ represents the capacitive and diffusive effect, respectively. Figure 4g describes the log($i$) vs. log($v$) plots of the 1.7 V/1.3 V redox couples (second cycle in CV), where b values are ~0.94 and ~0.84 for peak-a (anodic, 1.3 V) and peak-b (cathodic, 1.7 V) respectively which is tabulated in Table S1, suggesting the electrochemical process of NC@MoSe$_2$@rGO governed by pseudo capacitance.[48] The pseudocapacitive nature increases as the scan rate increases for the anode material[30] (inset, Figure 4g).

It was found that for 0.2 mVs$^{-1}$, 0.4 mVs$^{-1}$, 0.6 mVs$^{-1}$, 0.8 mVs$^{-1}$ and 1.0 mVs$^{-1}$, the capacitive contributions were ~33.8%, ~41.9%, ~46%, ~50.5%, ~53.3% respectively (all parameters and corresponding plot are shown in Figure S4 and Table S1&S2).

To understand the better electrochemical performance of NC@MoSe$_2$@rGO, Electrochemical Impedance Spectroscopy (EIS) were measured and compared with the NC@MoSe$_2$ electrode at OCV. As shown, the Nyquist plot of both electrodes (Figure S3g) are composed of electrode/electrolyte resistance from bulk ($R_1$), resistance near SEI layers ($R_2$) and charge transfer resistance ($R_3$) in the interface of the electrode. Based on the equivalent circuit model (Figure S3h), it has been found the lower SEI resistance and charges transfer resistance (~3.3 and 75.2 Ω) of the NC@MoSe$_2$@rGO compared to NC@MoSe$_2$ electrode (~9 and 167 Ω) in the higher and medium frequency region, respectively. Thus, the anode's high capacitive contribution can be speculated for the following reasons, as illustrated in Figure 4h. These are- (i) uniformly distributed MoSe$_2$ nanosheets reduces the internal resistance and increase faster diffusion of Na-ion due to direct access of electrolyte through NC compound, (ii) the structural strain of MoSe$_2$ could be minimized due to high surface area of NC and rGO (iii) Synergetic effect between active material with carbon through Mo−O−C bond, (iv) nitrogen-doped carbon could increase the conductivity of the electrode material and thus improve the electrochemical performance.[16]

Ex-situ SEM and EDAX mapping of the bare MoSe$_2$ and NC@MoSe$_2$@rGO electrode was done to investigate the structural stability of NC@MoSe$_2$ compound (in Figure S5) along with the N and Se$^-$ interaction. For bare MoSe$_2$ electrode, the elemental mapping shows less amount of the constituent discharge products (especially Se) (Figure S5a–c), whereas in NC@MoSe$_2$@rGO electrode, high active materials retention has been found after 50th cycle (Figure S5d–f). This could be due to the strong chemical interaction of doped carbon with the discharge products during cycling. Simultaneously, the smooth surface with well-maintained morphology of the active material and the residual electrolytes (existence of F, Cl, etc.) are shown in EDAX and elemental mapping in Figure. S5e indicates less volume discrepancy of MoSe$_2$ during cycling. The same interpretation can be explained from the HRXPS of N1s. As shown in Figure S6, the shift of pyridinic and pyrrolic N towards the lower binding energy (397.3 eV and 398.8 eV, respectively) compared to the fresh electrode (Figure 3e) implies the electron transfer from Se$^{n-}$ to the N atoms present on the carbon surface during cycling.[17,49]

## 2.3. Understanding the Na$^+$ Storage Behavior of MoSe$_2$ Electrode

The ex-situ X-ray absorption near the edge (XANES) and Extended X-ray absorption fine structure (EXAFS) experiments were performed in fluorescence mode at the Energy Scanning EXAFS beamline (BL-9) at Indus-2 Synchrotron source, Raja Ramanna Centre for Advanced Technology (RRCAT), Indore.

**Batteries & Supercaps**

Articles
doi.org/10.1002/batt.202100026

Chemistry
Europe

European Chemical
Societies Publishing

The detailed beamline specifications are discussed in the supporting information and our earlier publications.[50–52]

For ex-situ Mo and Se K-edge measurements, the cells were cycled at different discharge/charge potentials at a current density of 20 mA g$^{-1}$. After the electrochemical measurements, the cells were disassembled inside the Ar-filled glove box to avoid atmospheric oxygen's direct contact to minimize the surface oxidation and moisture content. The electrodes were washed with the electrolyte solvent inside the glove box to remove the salts and sealed with adhesive Kapton tape and taken for XAS measurements. Mo K-edge XANES on the $MoSe_2$ electrodes during the electrochemical charge/discharge process against sodium were performed after full discharge, after the 1$^{st}$ cycle. The XAS data were recorded for the cycled electrodes along with the pristine $MoSe_2$ and Mo foil. Figure 5(a) presents the normalized Mo K-edge XANES spectra for $MoSe_2$ cycled electrodes, i.e., after first discharge 1$^{st}$ charge state along with pristine $MoSe_2$ and Mo foil. The wiggles/oscillatory features of the post-edge region of XANES spectra provide information about the nearest neighbours and the local chemistry. The inset of Figure 5 (a) shows post-edge areas of the Mo XANES spectra, where Mo foil has features of six picks at 20013.7, 20038.6, 20061.9, 20083.3, 20123.8, 20190.6 eV (also in Figure S7 (a)) denoted as $Mo_1$, $Mo_2$, $Mo_3$, $Mo_4$, $Mo_5$ and $Mo_6$, respectively.[53] Similarly, for pristine $MoSe_2$, the peaks positioned at 20031.9, 20054.9, 20105.2, 20166.9 eV, denoted as $P_1$, $P_2$, $P_3$, $P_4$, respectively. It has been observed that for the electrode after the full discharge process, the characteristic
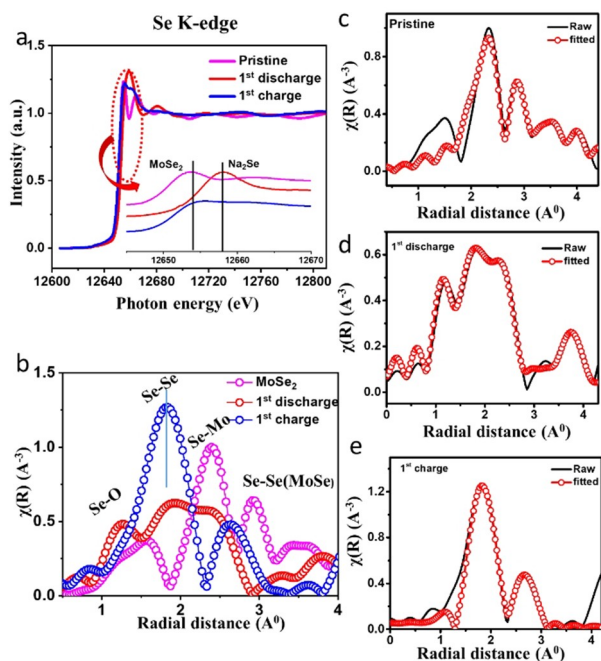
oscillatory peak features of $MoSe_2$ diminishes with the increase in Na$^+$ concentration.

In contrast, the distinctive post edge oscillatory components ($Mo_1$ and $Mo_2$) of Mo foil XANES became more prominent. This is due to a decrease in the interaction between Mo and Se atoms as the concentration of Na$^+$ increases. Finally, the post edge oscillatory features match with that of the standard Mo foil. This indicates the conversion of the $MoSe_2$ phase to the metallic Mo nanoparticle after the full discharge process of the $MoSe_2$ electrode. For the electrode after the 1$^{st}$ cycle, the oscillatory peak features slightly matches with the $MoSe_2$.

We plotted corresponding FT-EXAFS in R space shown in Figure 5b. It should be noted that the actual bond length and the peak positions in the R space are differed by ~0.3 to 0.5 Å depending on the type of nearest neighbour scatterer. The major intense peaks for $MoSe_2$ are at ~2.09 Å, and ~2.99 Å corresponds to the first nearest Mo–Se single scattering (SS) and Mo–Mo SS path, respectively. However, after the first discharge process, the bond distance of Mo–Se and Mo–Mo shifted to ~1.97 Å and ~2.72 Å, respectively, with low intensities. The decreasing intensities refer to the conversion reaction of $MoSe_2$. Simultaneously, the peak appeared at ~1.12 Å matches with the nearest Mo–O SS path from the $MoO_3$ structure. After the end of the first cycle (1$^{st}$ charge), the Mo–Se bond distance increases to ~2.11 Å compared to the bond distance at discharge state. However, the Mo–O bonds still present at ~1.1 Å. The peak intensity does not recover to the pristine $MoSe_2$ due to the transformation from bulk to nanomaterial with amorphous phases. The same observation has been found in the CV data. Finally, fitting of the pristine, first discharge and first charged samples obtained by experiments were carried out (as shown in Figure 5(c)–(e)) with the theoretical data of $MoSe_2$ and $MoO_3$. The best-fitting parameters are presented in Table S3. Along with the Mo edge, we have performed the same experiment for the Se K edge, as shown in Figure 6a. Pristine $MoSe_2$ exhibits a sharp peak at 12652.6 eV with some shoulder at higher energy due to Se 3p orbital antibonding with Mo 4d states. The same phenomena reported for $MoS_2$ also.[54] After 1$^{st}$ discharge process, the feature of $MoSe_2$ has disappeared, and a peak at 12653.2 eV starts appearing. This peak can be correlated with the formation of $Na_2Se$.[55] The spectra change entirely during the charging process, and the fingerprint of $MoSe_2$ still present after 1$^{st}$ charge (inset of Figure 6(a)). When EXAFS data were plotted in R space, pristine material shows the most intense peak at ~2.38 Å and ~2.95 Å that is due to the first SS of Se–Mo and Se–Se path, respectively. After the 1$^{st}$ discharge process, the peaks are located at ~1.24 Å, ~1.89 Å and ~2.45 Å. The peak at ~1.24 Å is due to Se-compound's air oxidation to form Se–O bond and could only be fitted if the Se–O path from $SeO_2$ (fitted parameters are tabulated in Table S4). The other two peaks are fitted with SS of Se–Se from Se and Se–Mo from $MoSe_2$. By taking consideration of the bond length of Se–Mo in pristine and 1$^{st}$ discharge process, the bond length shifted to the higher value (~2.38 Å, pristine vs. ~2.45 Å) after 1$^{st}$ discharge process of $MoSe_2$ electrode, which is due to the
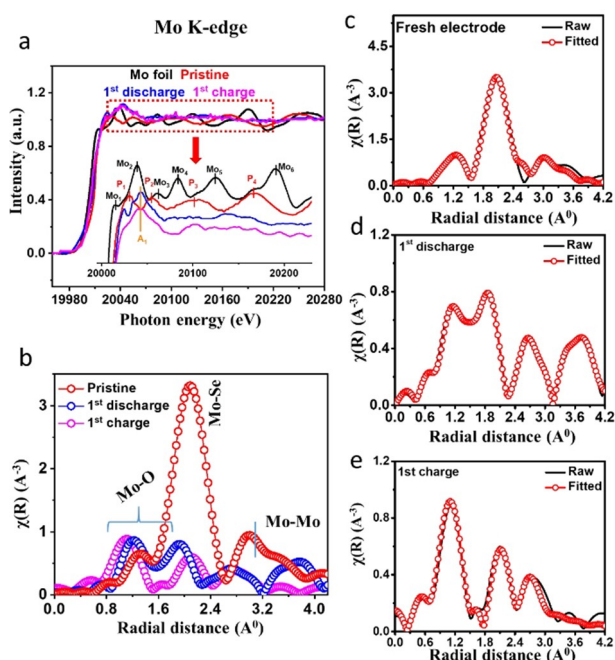


**Figure 5.** a) Normalized XANES spectra of $MoSe_2$ (Mo K-edge) at different cycles, b) combine experimental χ(R) versus R spectra of all the samples with different electrochemical states, Normalized EXAFS spectra with Fourier transformed magnitude along with the best fit theoretical plot of) as-prepared $MoSe_2$, d) after 1$^{st}$ discharge and e) 1$^{st}$ charge process.

**Batteries & Supercaps**

Articles
doi.org/10.1002/batt.202100026

Chemistry
Europe
European Chemical
Societies Publishing



**Figure 6.** a) Normalized XANES spectra of MoSe$_2$ (Se K-edge) at different cycles, b) combine experimental $\chi(R)$ versus R spectra of all the samples with different electrochemical states, normalized EXAFS spectra with Fourier transformed magnitude along with the best fit theoretical plot of c) as-prepared MoSe$_2$, d) after 1$^{st}$ discharge and e) 1$^{st}$ charge process.
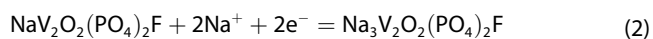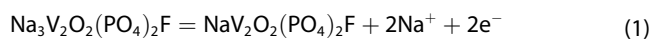
conversion of MoSe$_2$ at with the increasing concentrations of Na$^+$ at lower discharge voltage. After the 1$^{st}$ cycle charge process, an intense high peak at ~1.83 Å is due to the formation of a Se—Se bond from Se (in Figure 6b and S7b). Simultaneously, the low intense peak of ~2.58 Å has been observed, which can be fitted by considering the SS path of Se—Se in MoSe$_2$. The shallow intense peaks after ~3.0 Å has observed after the first cycle (full charge state), which can be correlated with the formation of Na—Se bond, as Na$_2$Se$_x$ during cycling. The fitting of the pristine, first discharge, and first charged samples were carried out (as shown in Figure 6(c)–(e)) with the reference of standard theoretical data of MoSe$_2$ and SeO$_2$, Se and Na$_2$Se, respectively. The best-fitting parameters are presented in Table S4. A similar observation has been found from the ex-situ XPS studies of the cycled electrodes. As shown in Figure S8a, at OCV, Mo 3d spectra show two splitting at ~228 eV and ~231.0 eV, for Mo 3d$_{5/2}$ and Mo 3d$_{3/2}$, respectively as mentioned previously. After 1$^{st}$ discharge at 0.1 V, Mo's oxidation states have increased as it formed Mo nanoparticle, which oxidized during sample preparation. As a result, the appearance of new peak Mo 3d$_{5/2}$ appeared at ~235 eV. The HRXPS of Se 3d (in Figure S9b) shows shifting of peaks at higher binding energy after 1$^{st}$ discharge process as compared to pristine (53.8 eV to 54.4 eV and 54.7 eV to 55.3 eV for Se 3d$_{5/2}$ and Se 3d$_{3/2}$, respectively). This is due to a change in the environment of Se after full discharge process. The peak at ~59.1 eV and ~63 eV was due to air-oxidation of Na$_2$Se[56] and Na 2 s,[57] respectively. This confirms the formation of Mo and Na$_2$Se at the end of the full discharge process. During the charging process, both Mo 3d and Se 3d peaks remain the

same as the peaks after the 1$^{st}$ discharge process, suggesting the reformation of MoSe$_2$ is negligible after the first cycle.

The XANES, EXAFS and XPS results confirm the formation of different charged products after the first cycle. We have found that as the concentration of Na$^+$ increases, the spectra of the electrode material matches with the XANES and EXAFS spectra of standard foil of Mo and Se. After a full discharge process, the formation of Mo nanoparticles and the Na$_2$Se have been confirmed by XPS. While charging, weak features of MoSe$_2$ can be detected. This could be due to the unreacted active materials. We are currently working on the in-depth DFT analysis to understand the reaction mechanism after a few cycles.

### 2.4. Full-Cell Study of NC@MoSe$_2$@rGO//NVOPF

An excellent promising cathode material can provide high energy density to the battery with high specific capacity and high redox potentials. Herein, we have adopted polyanion based cathode- sodium vanadium fluorophosphate (Na$_3$V$_2$O$_2$(PO$_4$)$_2$F, denoted as NVOPF) as a cathode material to construct the full cell against NC@MoSe$_2$@rGO anode. The inductive effect of the (PO$_4$)$^{3-}$and electronegative fluorine can provide a high theoretical specific capacity of ~128 mA h g$^{-1}$ with the average potential of ~3.9 V. Physical characterizations such as- XRD determined the crystal structure of as-synthesized NVOPF and its well-matched with the tetragonal NVOPF (PDF#97-041-1950) (Figure S9(a) (fitted parameters are shown in Table S5). Raman peaks at 380.1, 942.9 and 1050 cm$^{-1}$ attributed (Figure S9 (b)) to the $v_1$, $v_2$ and $v_3$ vibration mode of the PO$_4$$^{3-}$ anion in the cathode structure.[58,59] Two prominent peaks at 942.9 and 1050 cm$^{-1}$ are because of the symmetric A$_{1g}$ stretching of P—O bond and antisymmetric stretching of PO43$^-$ anion. SEM and TEM images show the cubic morphology of NVOPF with average size of ~250 nm (Figure S9c, d). EDAX and mapping (Figure S9e and f) confirm the uniform distribution of Na, V, F, and P in the cathode structure. The electrochemical performance of NVOPF material tested against Na-ion half-cell within a potential window of 3.0 V to 4.5 V. The CV plot in Figure S10 (g) shows two redox couples at 3.7 V/3.4 V and 4.0 V/3.9 V *vs* Na/Na$^+$, corresponding to V$^{4+}$ and V$^{5+}$ couple.[60,61] The anodic peaks are due to the conversion of V$^{4+}$ to V$^{5+}$ cathodic peaks related to the insertion of Na-ion into the NVOPF active materials. The reactions are as follows during (de)-sodiation process [Eqs. (1), (2)]:[61]

$$Na_3V_2O_2(PO_4)_2F = NaV_2O_2(PO_4)_2F + 2Na^+ + 2e^- \qquad (1)$$

$$NaV_2O_2(PO_4)_2F + 2Na^+ + 2e^- = Na_3V_2O_2(PO_4)_2F \qquad (2)$$

The corresponding GCD profiles and cyclic stability are illustrated in Figure S10h and i at a current density of 0.2 C (1 C = 130 mA h g$^{-1}$, 2 Na$^+$ per formula unit) rates. It delivers the initial charge capacity of 137.6 mA h g$^{-1}$ with a Coulombic efficiency of ~71%. After 50$^{th}$ cycles, it shows a charge capacity of ~89.0 mA h g$^{-1}$ with an efficiency of 93.5%. During the

**Batteries & Supercaps**

Articles
doi.org/10.1002/batt.202100026

**Chemistry
Europe**
European Chemical
Societies Publishing

charge and discharge process, the two distinct plateaus were observed at 3.7 V/4.1 V and 3.9 V/3.5 V, respectively, which agrees with the CV profile as discussed earlier. So, the cathode exhibits good cycle life against sodium-ion.

After observing the individual performances of NVOPF cathode and NC@MoSe$_2$@rGO anode, we designed the full-cell of NC@MoSe$_2$@rGO//NVOPF (as schematically illustrated in Figure 7a). The mass ratio of active materials was about (cathode/anode material) 3:1. Firstly, before assembly the full-cell, the anode put direct contact with Na-foil, dipped in the electrolyte, and kept for sufficient time to allow the formation of SEI layers on the anode surface chemically. It is always necessary to fix the limit of the higher-cut potential during the full-cell charge to avoid the platting of sodium on the anode surface. Here, we checked the electrochemical performances of the full-cells in three different potential windows: Case I: 1.5 V to 4.0 V, Case II: 1.5 V to 4.0 V (only first cycle) and 1.5 V to 3.5 V (from the second cycle onwards) and Case III: 1.5 V to 3.5 V, by keeping the current density, weight of active material identical to understand the utilization of anode material at the higher potential. Here all the capacities and current rates are calculated based on the anode mass loading on the electrode.

For case, I, (Figure S10a, inset), the first cycle oxidation peaks was found to be at ~3.2 V and ~3.6 V, which is maybe due to intercalation and conversion of anode material, respectively (based on first oxidation and reduction peak of individual cathode and anode respectively). According to the half-cell reaction of the anode side, less than two Na$^+$ can insert during the intercalation reaction, and a maximum of four Na$^+$ can involve during conversion to form Mo and Na$_2$Se in the first cycle. Similarly, two Na + involvement is there during the first cycle of charging/discharging on the cathode side. The first reduction peak at ~1.8 V signifies the intercalation of sodium-ion into the cathode and transformation of NaV$_2$O$_2$(PO$_4$)$_2$F into its original structure Na$_3$V$_2$O$_2$(PO$_4$)$_2$F. The second cycle onwards, fixed redox peaks were found at ~2.1 V

(oxidation) and ~1.8 V (reduction). The proposed full-cell reaction mechanism as follows [Eq. (3)]:

$$2Na_3V_2O_2(PO_4)_2F + MoSe_2 = 2Na_3V_2O_2$$
$$(PO_4)_2F + Mo + 2Na_2Se \tag{3}$$
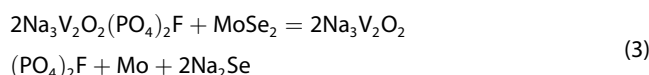
The GCD profile (Figure S10b) shows the initial charge, and the discharge capacity was ~563 mAhg$^{-1}$ and ~391 mAhg$^{-1}$ at a current density of 50 mAg$^{-1}$. After the end of the 50$^{th}$ cycle, the capacity decayed to ~225 mAhg$^{-1}$, with capacity retention was only ~47%. Figure S10c and d show the full-cell's stability and GCD plot according to Case II. In this case, the cell was first charged to 4.0 V for the only first cycle to ensure the complete conversion of MoSe$_2$ to Mo and Na$_2$Se, and then after the second cycle, the higher potential was restricted to 3.5 V to get the stability of the cell. The initial charge capacity remains high (~568 mAhg$^{-1}$) because of its higher cut-off potential at 4.0 V. After initial stabilization, the full-cell shows a charge capacity of ~269 mAhg$^{-1}$ (3$^{rd}$ cycle) with an increasing Coulombic efficiency of ~73%. It was found that capacity retention was increased from ~47.8% (Case I) to ~54.4%. The overall charge capacity was ~187 mAhg$^{-1}$ and ~147 mAhg$^{-1}$ after 50 cycles. So, capacity retention was improved when the full-cell's higher potential came down from 4.0 V to 3.5 V. To improve the full-cell's cyclic constancy we fixed our battery working potential at the range of 1.5 V–3.5 V (Case III). Figure 7b shows the first oxidation/reduction peak at ~3.26 V/~1.8 V. The peak ~3.26 V probably represents the intercalation of Na$^+$ from the cathode side to anode side to form Na$_x$MoSe$_2$ and cathode transform to NaV$_2$O$_2$(PO$_4$)$_2$F. The full-cell's excellent reversibility and stability have been observed from the second cycle onwards with a constant redox couple of 2.2 V/1.8 V. The 2$^{nd}$ cycle comparison of GCD plot (Figure 7c) of the cathode, anode, and full-cell at the same current density of 50 mAg$^{-1}$. It can be seen that cathode and anode working potential was ~3.6 V and ~1.5 V, respectively; that is why we can achieve the sodium-ion full-cell potential of ~2.1 V. The excellent cyclic stability of full-cell prototype up-to 100 cycles at a current density of 50 mAg$^{-1}$, shown in Figure 7(d) where initial discharge capacity of 200 mAhg$^{-1}$ with a Coulombic efficiency of ~66%. It delivers the reversible specific capacity of 176 mAhg$^{-1}$ with a Coulombic efficiency of ~92.7% and capacity retention of ~83%. Figure 7(e) displays the full-cell's power plot within the same potential window at various current rates. The specific discharge capacities of ~286.7 mAhg$^{-1}$, ~222.0 mAhg$^{-1}$, 180.8 mAhg$^{-1}$, 160.3 mAhg$^{-1}$ were achieved at a current density of 25 mAg$^{-1}$, 50 mAg$^{-1}$, 75 mAg$^{-1}$ and 100 mAg$^{-1}$, respectively. The full-cell retained its capacities ~189.5 8 mAhg$^{-1}$ when current density back to 50 mAg$^{-1}$ after 60 cycles. These results indicate the high-power capability of the NC@MoSe$_2$@rGO composite in the full-cell system. The detailed comparative study of sodium-ion full-cells reported previously has been tabulated with our finding in Table S7. For practical application, a light-emitting diode (LED) lamp was tested to lighten the connection of a single coin cell made by NVOPF cathode and NC@MoSe$_2$@rGO anode, as shown in Figure 7f. This high potential (~2.1 V)
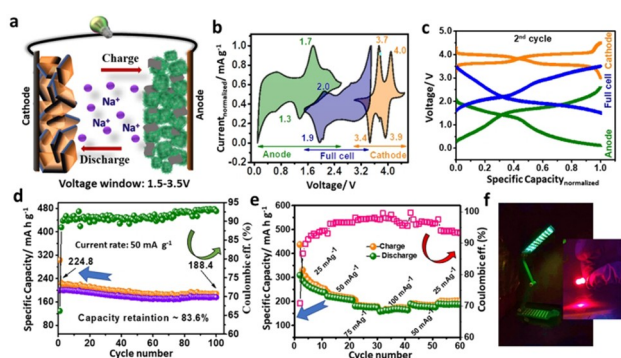


**Figure 7.** Electrochemical performance of sodium-ion full-cell NC@MoSe$_2$@rGO//NVOPF at 20 °C. a) Schematic illustration of the NVOPF as cathode and NC@MoSe$_2$@rGO as anode; b) CV plot between the potential range of 1.5 and 3.5 V; c) second cycle charge-discharge plot of individual cathode (orange), Full-cell (blue) and anode (green); d) Cyclic performance of the full-cell at a current rate of 50 mAg$^{-1}$; e) Rate performances at different current rates at 25, 50, 75 and 100 mAg$^{-1}$; f) demonstration of the lighting of LED study table lamp and LED bulb using our prototype.

sodium-ion full-cell technology (NC@MoSe$_2$@rGO//NVOPF) reflects MoSe$_2$ as a promising anode to store sodium-ion for both half and full-cell application.

## 3. Conclusions

In summary, NC@MoSe$_2$@rGO composite has been synthesized successfully using the solvothermal method, where NC and rGO compound increases the electronic conductivity, accommodates the volume expansion, and prevents the restacking during cycling. The NC@MoSe$_2$@rGO electrode exhibits superior electrochemical performance with a reversible capacity of ~391.8 mA h g$^{-1}$ (at 100 mA g$^{-1}$ over 120 cycles) provided excellent rate performances of ~194.2 mA h g$^{-1}$ at 1 A g$^{-1}$. The sodium storage mechanism has been investigated by ex-situ XANES, EXAFS and XPS studies, confirming the phase irreversibility after the first cycle. Lastly, to investigate the practical viability of sodium-ion full-cell battery, the NC@MoSe$_2$@rGO anode has tested against NVOPF cathode material with different upper cut-off potential to understand the sodiation processes in the anode side. Also, it has found from the CV experiment that above 3.5 V, anode behaves as a conversion-based material, and thus we achieve high capacity with low capacity retention. The capacity retention is increased from ~47% to ~83% after restricting the full-cell higher potential limit to 3.5 V to utilize anode as an intercalation-based material. Thus NC@MoSe$_2$@rGO//NVOPF full-cell showed the specific capacity of ~176 mA h g$^{-1}$ after the 100th cycle within the voltage window of 1.5–3.5 V. The full-cell system exhibits a high nominal potential of ~2.1 V with an energy density of ~369.6 Wh kg$^{-1}$ anode. Such results propose a MoSe$_2$ based anode that has a high potential for high-performance sodium-ion full-cell. The present study opens up to design different selenide based TMDs as an anode for sodium-ion battery. After the first cycle, an in-depth understanding of the sodiation mechanism could help understand the effect of active materials on sodiation behaviour.

## Experimental Section

### Chemicals

All reagents and solvents used for the synthesis of NC@MoSe$_2$@rGO and Na$_3$V$_2$O$_2$(PO$_4$)$_2$F (NVOPF) were used without further purification modification. The following chemicals were used- Sodium molybdate dihydrate (Na$_2$MoO$_4$, 2H$_2$O, 99.5%, Sigma-Aldrich), Se powder (~100 mesh, 99.99% trace element, Sigma), Ethylene Glycol (EG, Merck, 2.5 L), Zinc acetate dihydrate (Zn(CH$_3$COO)$_2$, 2H$_2$O, Sigma-Aldrich), 2-methylimidazole (AR, Sigma), glucose, Sodium fluoride (NaF, Spectrochem), Ammonium dihydrogen phosphate (NH$_4$H$_2$PO$_4$, Merck GR), Ammonium metavanadate (NH$_4$VO$_3$, Sigma). For electrolyte preparation, Sodium perchlorate (NaClO$_4$, 98%), Propylene carbonate (PC, 99.7% anhydrous), Ethylene carbonate (EC) and Fluoroethylene carbonate (FEC) were obtained from Aldrich, India. Na metal (>99% metal basis) Super P were obtained from Sigma Aldrich, India and Timcal, Switzerland.

### Synthesis of ZIF-8, NC, and NC@MoSe$_2$@rGO

Zeolite Imidazole Framework (ZIF-8) was synthesized through a modified procedure reported elsewhere.[62] Typically, zinc acetate dihydrate and 2-methylimidazole powders were dissolved separately in 150 ml deionized solution at a weight ratio of 1:3 and wait till clear solution. Both solutions were mixed with continuous stirring for one hour and aged for one day until a white precipitate formed. Next, it was washed several times with deionized water and kept drying in an air oven for 12 h at 65 °C. Carbonization of ZIF-8 powder was done at high temperature (850 °C) for 1 h in an inert atmosphere at a heating rate of 5 °C min$^{-1}$. The black carbonized powders (NC) were then refluxed with HCl solution to remove the residual by-products. After that, final products were washed with DI water followed by drying in an air oven at 65 °C for 12 h. NC@MoSe$_2$@rGO were prepared through the solvothermal method. In this process, two mmol of Na$_2$MoO$_4$, 2H$_2$O, 50 mg of NC, and GO were dissolved in a mixture of 20 ml ethylene glycol and a 0.05 M (25 ml) glucose solution magnetic stirring. In another beaker, Se powder was dissolved in 20 ml N$_2$H$_4$ until a dark brown solution formed. Finally, two solutions were mixed, transferred into a 100 mL Teflon-lined autoclave, and kept at 200° C for 12 h. After the furnace's natural cooling, the black colour product was collected by washing with ethanol followed by centrifugation at 8000 rpm for 30 min. The as-prepared sample was further treated at 800 °C for 1 h to obtain high crystalline NC@MoSe$_2$@rGO. The same technique mentioned above was followed to prepare only MoSe$_2$ and NC individual without the addition of ZIF-8 and MoSe$_2$, respectively, before heat treatment.

### Synthesis of NVOPF

Na$_3$V$_2$O$_2$(PO$_4$)$_2$F (NVOPF) nano-boxes were prepared via a simple solvothermal process.[60,61] Firstly, NH$_4$VO$_3$, NH$_4$H$_2$PO$_4$ and Fluoride sources (NaF) were dissolved in deionized water with an appropriate molar ratio to form a clear solution. After that, solution was added to a DMF solution at 80 °C for 45 min. The homogeneous solution was sealed in a 100 ml Teflon-lined autoclave for 180 °C for 24 hr. Next, the obtained residue was washed several times with water and ethanol and kept for vacuum drying at 60 °C for 24 hr.

### Physical Characterization

Rigaku Smartlab Diffractometer ($\lambda = 1.5418$ Å) was used for Powder X-ray diffraction (XRD) measurements of the MoSe$_2$@ZIF and NVOPF 27 °C at 40 kV and 40 mA, within a 2θ range of 10 to 70. Laser Raman confocal spectroscopy [HORIBA LabRAM HR800-UV spectrometer, a laser source of 532 nm, at 50 mW] were used to identify the phase (the range used for the experiment was between 100 to 1000 cm$^{-1}$). Furthermore, Field emission gun scanning (Ultra 55 FE-SEM, ZEISS) and transmission electron microscopy (TEM) (FEI Tecnai, 300 kV) analysis were carried out to examine the morphology. Fourier transformed IR (NICOLET 8700) and X-ray photoelectron spectroscopy (XPS; AXIS Supra, Kratos Analytical, monochromatic) study was carried out in High-resolution mood. TGA of the composite powder was done using TA Q600 instrument from RT to 800 °C with the scan rate of 10 °C/min in air.

### Electrochemical Characterization

The cathode and anode were tested individually in a half-cell configuration to check the electrochemical performances. For half-cell, as prepared, NC@MoSe$_2$@rGO anode powder mixed with PVDF binder and conductive carbon at a ratio of 70: 20: 10 in NMP based

**Batteries & Supercaps**

Articles
doi.org/10.1002/batt.202100026

**Chemistry Europe**
European Chemical
Societies Publishing

solvent. After that, the black colour slurry was cast on Cu-foil and kept for drying before used as a working electrode (WE). Similarly, cathode slurry was prepared at the same ratio and cast onto Al-foil. The average total mass loading obtained ~2.2 mg/cm$^2$ for cathode and ~1.1 mg/cm$^2$ for the anode. For a full-cell, the mass ratio of positive to negative is set to 3:1 to utilize the whole active material. The Galvanostatic charge-discharge (GCD) tests were performed using a 2032 type coin cell inside the argon-filled glove box. Na metal (Alfa Aesar, 99.8%) was used as a reference electrode (RE). 1 M NaClO$_4$ in EC: PC (1:1 vol %) with 5% FEC used as an electrolyte. Electrolyte soaked borosilicate glass fibre (Whattman) was placed between the cathode and anode before assembling the cells. Bio-logic VMP-3 was used to perform the impedance, and cyclic voltammetry (CV) tests at a scan rate of 0.1 mV S$^{-1}$ (anode and cathode potential range 0.1–2.6 V and 3.0 V −4.5 V, respectively). For full-cells, the anode was allowed to contact Na-foil in the presence of the electrolyte and kept for 30 min for the formation of stable SEI on the anode surface.[63] After that, it was assembled with active cathode material. The as-prepared full-cell were tested 1.5 V to 4.0 V and 1.5 V to 3.5 V to understand the full-cell's proper voltage window. Electrochemical charge-discharge experiments were performed using an Arbin testing instrument (BT2000, USA) at the same potential widow with various current rates to check the as-prepared cells' durability and cyclability. All the electrochemical experiments were carried out at a constant temperature of 20 °C. RT.

## Acknowledgements

## Conflict of Interest

The authors declare no conflict of interest.

[1] K. Chang, W. Chen, *J. Mater. Chem.* **2011**, *21*, 17175.
[2] X. Li, W. Li, M. Li, P. Cui, D. Chen, T. Gengenbach, L. Chu, H. Liu, G. Song, *J. Mater. Chem. A* **2015**, *3*, 2762.
[3] Y. Y. Lee, G. O. Park, Y. S. Choi, J. K. Shon, J. Yoon, K. H. Kim, W. S. Yoon, H. Kim, J. M. Kim, *RSC Adv.* **2016**, *6*, 14253.
[4] Z. Zhang, X. Yang, Y. Fu, K. Du, *J. Power Sources* **2015**, *296*, 2.
[5] Y. Li, Y. Lu, C. Zhao, Y. S. Hu, M. M. Titirici, H. Li, X. Huang, L. Chen, *Energy Storage Mater.* **2017**, *7*, 130.
[6] Y. Wu, M. Xu, X. Chen, S. Yang, H. Wu, J. Pan, X. Xiong, *Nanoscale* **2016**, *8*, 440.
[7] C. Dai, E. Qing, Y. Li, Z. Zhou, C. Yang, X. Tian, Y. Wang, *Nanoscale* **2015**, *7*, 19970.
[8] S. Tongay, J. Zhou, C. Ataca, K. Lo, T. S. Matthews, J. Li, J. C. Grossman, J. Wu, *Nano Lett.* **2012**, *12*, 5576.
[9] C. P. Yang, Y. X. Yin, Y. G. Guo, *J. Phys. Chem. Lett.* **2015**, *6*, 256.
[10] Y. Pang, S. Zhang, L. Liu, J. Liang, Z. Sun, Y. Wang, C. Xiao, D. Ding, S. Ding, *J. Mater. Chem. A* **2017**, *5*, 17963.
[11] D. Xie, W. Tang, Y. Wang, X. Xia, Y. Zhong, D. Zhou, D. Wang, X. Wang, J. Tu, *Nano Res.* **2016**, *9*, 1618.
[12] J. Zhang, M. Wu, T. Liu, W. Kang, J. Xu, *J. Mater. Chem. A* **2017**, *5*, 24859.
[13] A. Roy, P. K. Dutta, S. Mitra, *J. Mater. Chem. A* **2017**, *5*, 20491.
[14] Y. Dou, Y. Wang, D. Tian, J. Xu, Z. Zhang, Q. Liu, B. Ruan, J. Ma, Z. Sun, S. X. Dou, *2D Mater.* **2017**, *4*, 015022.
[15] S. H. Choi, Y. C. Kang, *ACS Appl. Mater. Interfaces* **2015**, *7*, 24694.
[16] C. Z. Y. Lin, Z. Qiu, D. Li, S. Ullah, Y. Hai, H. Xin, W. Liao, B. Yang, H. Fan, J. Xu, *Energy Storage Mater.* **2018**, *11*, 67.
[17] F. Niu, J. Yang, N. Wang, D. Zhang, W. Fan, J. Yang, Y. Qian, *Adv. Funct. Mater.* **2017**, *27*, 1700522(1.
[18] A. Roy, A. Ghosh, A. Kumar, S. Mitra, *Inorg. Chem. Front.* **2018**, *5*, 2189.
[19] C. Luo, Y. Xu, Y. Zhu, Y. Liu, S. Zheng, Y. Liu, A. Langrock, C. Wang, *ACS Nano* **2013**, *7*, 8003.
[20] J. Li, H. Hu, F. Qin, P. Zhang, L. Zou, H. Wang, K. Zhang, Y. Lai, *Chem. A Eur. J.* **2017**, *23*, 14004.
[21] X. Yang, Z. Zhang, X. Shi, *J. Alloys Compd.* **2016**, *686*, 413.
[22] F. Zheng, W. Zhong, Q. Deng, Q. Pan, X. Ou, Y. Liu, X. Xiong, C. Yang, Y. Chen, M. Liu, *Three-dimensional (3D) flower-like MoSe 2 /N-doped carbon composite as a long-life and high-rate anode material for sodium-ion batteries*, Vol. 357 **2019**, pp. 226–236.
[23] Y. Zhao, Z. Song, X. Li, Q. Sun, N. Cheng, S. Lawes, X. Sun, *Energy Storage Mater.* **2016**, *2*, 35.
[24] B. Ma, P. Y. Guan, Q. Y. Li, M. Zhang, S. Q. Zang, *ACS Appl. Mater. Interfaces* **2016**, *8*, 26794.
[25] M. Zhang, Q. Dai, H. Zheng, M. Chen, L. Dai, *Adv. Mater.* **2018**, *30*, 1.
[26] Y. Guo, J. Tang, H. Qian, Z. Wang, Y. Yamauchi, *Chem. Mater.* **2017**, *29*, 5566.
[27] H. L. Jiang, B. Liu, Y. Q. Lan, K. Kuratani, T. Akita, H. Shioyama, F. Zong, Q. Xu, *J. Am. Chem. Soc.* **2011**, *133*, 11854.
[28] Y. V. Kaneti, J. Zhang, Y. B. He, Z. Wang, S. Tanaka, M. S. A. Hossain, Z. Z. Pan, B. Xiang, Q. H. Yang, Y. Yamauchi, *J. Mater. Chem. A* **2017**, *5*, 15356.
[29] M. Du, D. Song, A. Huang, R. Chen, D. Jin, K. Rui, C. Zhang, J. Zhu, W. Huang, *Angew. Chem. Int. Ed.* **2019**, *58*, 5307.
[30] Q. Zhang, Y. Zhou, F. Xu, H. Lin, Y. Yan, K. Rui, C. Zhang, Q. Wang, Z. Ma, Y. Zhang, K. Huang, J. Zhu, W. Huang, *Angew. Chem. Int. Ed.* **2018**, *57*, 16436.
[31] Y. Liu, M. Zhu, D. Chen, *J. Mater. Chem. A* **2015**, *3*, 11857.
[32] W. Zhou, Z. Yin, Y. Du, X. Huang, Z. Zeng, Z. Fan, H. Liu, J. Wang, H. Zhang, *Small* **2013**, *9*, 140.
[33] X. Xu, Z. Fan, X. Yu, S. Ding, D. Yu, X. Wen, D. Lou, *Adv. Energy Mater.* **2014**, *4*, 2.
[34] J. C. Shaw, H. Zhou, Y. Chen, N. O. Weiss, Y. Liu, Y. Huang, X. Duan, *Nano Res.* **2014**, *7*, 1.
[35] Z. Liu, Y. Zhang, H. Zhao, N. Li, Y. Du, *Sci. China Mater.* **2017**, *60*, 167.
[36] X. Yang, Z. Zhang, Y. Fu, Q. Li, *Nanoscale* **2015**, *7*, 10198.
[37] C. Dai, Z. Zhou, C. Tian, Y. Li, C. Yang, X. Gao, X. Tian, *J. Phys. Chem. C* **2017**, *121*, 1974.
[38] T. Xiang, S. Tao, W. Xu, Q. Fang, C. Wu, D. Liu, Y. Zhou, A. Khalil, Z. Muhammad, W. Chu, Z. Wang, H. Xiang, Q. Liu, L. Song, *ACS Nano* **2017**, *11*, 6483.
[39] G. Zhou, D. W. Wang, L. C. Yin, N. Li, F. Li, H. M. Cheng, *ACS Nano* **2012**, *6*, 3214.
[40] Y. Teng, H. Zhao, Z. Zhang, Z. Li, Q. Xia, Y. Zhang, L. Zhao, X. Du, Z. Du, P. Lv, K. Świerczek, *ACS Nano* **2016**, *10*, 8526.
[41] K. Share, A. P. Cohn, R. Carter, B. Rogers, C. L. Pint, *ACS Nano* **2016**, *10*, 9738.
[42] X. Zhao, W. Cai, Y. Yang, X. Song, Z. Neale, H. E. Wang, J. Sui, G. Cao, *Nano Energy* **2018**, *47*, 224.
[43] P. Ge, H. Hou, C. E. Banks, C. W. Foster, S. Li, Y. Zhang, J. He, C. Zhang, X. Ji, *Energy Storage Mater.* **2018**, *12*, 310.
[44] S.-K. Park, J. Lee, S. Bong, B. Jang, K. Seong, Y. Piao, *ACS Appl. Mater. Interfaces* **2016**, *8*, 19456.
[45] W. Ren, H. Zhang, C. Guan, C. Cheng, *Adv. Funct. Mater.* **2017**, *27*, 1.
[46] D. Su, D. Dou, G. Wang, *Adv. Energy Mater.* **2015**, *5*, 1.
[47] M. S. Raj, A. Panda Manas, D. Dimple, *Carbon* **2019**, *143*, 402.
[48] J. Gao, Y. Li, L. Shi, J. Li, G. Zhang, *ACS Appl. Mater. Interfaces* **2018**, *10*, 20635.
[49] J. P. Song, L. Wu, L. Da Dong, C. F. Li, L. H. Chen, X. Dai, C. Li, H. Chen, W. Zou, W. B. Yu, Z. Y. Hu, J. Liu, H. E. Wang, Y. Li, B. L. Su, *Nanoscale* **2019**, *11*, 6970.
[50] M. Adil, A. Sarkar, A. Roy, M. R. Panda, A. Nagendra, S. Mitra, *ACS Appl. Mater. Interfaces* **2020**, *12*, 11489.
[51] U. K. Sen, P. Johari, S. Basu, C. Nayak, S. Mitra, *Nanoscale* **2014**, *6*, 10243.

[52] M. R. Panda, R. Gangwar, D. Muthuraj, S. Sau, D. Pandey, A. Banerjee, A. Chakrabarti, A. Sagdeo, M. Weyland, M. Majumder, Q. Bao, S. Mitra, *Small* **2020**, *16*, 1.

[53] Z. Zhu, S. Xi, L. Miao, Y. Tang, Y. Zeng, H. Xia, Z. Lv, W. Zhang, X. Ge, H. Zhang, J. Wei, S. Cao, J. Chen, Y. Du, X. Chen, *Adv. Funct. Mater.* **2019**, *29*, 1.

[54] L. Zhang, D. Sun, J. Kang, J. Feng, H. A. Bechtel, L. W. Wang, E. J. Cairns, J. Guo, *Nano Lett.* **2018**, *18*, 1466.

[55] E. Curti, A. Froideval-Zumbiehl, I. Günther-Leopold, M. Martin, A. Bullemer, H. Linder, C. N. Borca, D. Grolimund, *J. Nucl. Mater.* **2014**, *453*, 98.

[56] S. Park, C. H. Champness, I. Shih, *J. Electron Spectrosc. Relat. Phenom.* **2015**, *205*, 23.

[57] V. Medabalmi, G. Wang, V. K. Ramani, K. Ramanujam, *Appl. Surf. Sci.* **2017**, *418*, 9.

[58] M. Xu, L. Wang, X. Zhao, J. Song, H. Xie, Y. Lu, J. B. Goodenough, *Phys. Chem. Chem. Phys.* **2013**, *15*, 13032.

[59] Y. Yin, F. Xiong, C. Pei, Y. Xu, Q. An, S. Tan, Z. Zhuang, J. Sheng, Q. Li, L. Mai, *Nano Energy* **2017**, *41*, 452.

[60] P. R. Kumar, Y. H. Jung, J. E. Wang, D. K. Kim, *J. Power Sources* **2016**, *324*, 421.

[61] H. Jin, J. Dong, E. Uchaker, Q. Zhang, X. Zhou, S. Hou, J. Li, G. Cao, *J. Mater. Chem. A* **2015**, *3*, 17563.

[62] R. Wang, D. Jin, Y. Zhang, S. Wang, J. Lang, X. Yan, L. Zhang, *J. Mater. Chem. A* **2017**, *5*, 292.

[63] A. Sarkar, C. V. Manohar, S. Mitra, *Nano Energy* **2020**, *70*, 104520.